Journal of the Korean Physical Society, Vol. 65, No. 12, December 2014, pp. 2111∼2116

Differential X-ray Phase-contrast Imaging with a Grating Interferometer Using a Laboratory X-ray Micro-focus Tube

Kwon-Ha Yoon,* Jong Hyun Ryu and Chang Won Jung
Department of Radiology and Imaging Science Research Center, Wonkwang University School of Medicine, Iksan 570-749, Korea

Cheol Woo Ryu, Young Jo Kim and Young Man Kwon
Radiation Imaging Technology Center, Jeonbuk Technopark, Iksan 570-802, Korea

Miran Park and Seungryong Cho
Department of Nuclear and Quantum Enginnering, Korea Advanced Institute of Science and Technology, Daejeon 305-701, Korea

Kwon Su Chon
Department of Radiological Science, Catholic University of Daegu, Gyeongsan 712-702, Korea

(Received 26 December 2013, in final form 20 October 2014)

X-ray phase-contrast imaging can provide images with much greater soft-tissue contrast than conventional absorption-based images. In this paper, we describe differential X-ray phase-contrast images of insect specimens that were obtained using a grating-based Talbot interferometer and a laboratory X-ray source with a spot size of a few tens of micrometers. We developed the interferometer on the basis of the wavelength, periods, and height of the gratings; the field of view depends on the size of the grating, considering the refractive index of the specimen. The phase-contrast images were acquired using phase-stepping methods. The phase contrast imaging provided a significantly enhanced soft-tissue contrast compared with the attenuation data. The contour of the sample was clearly visible because the refraction from the edges of the object was strong in the differential phase-contrast image. Our results demonstrate that a grating-based Talbot interferometer with a conventional X-ray tube may be attractive as an X-ray imaging system for generating phase images. X-ray phase imaging obviously has sufficient potential and is expected to soon be a great tool for medical diagnostics.

PACS numbers: 87.57.Gy, 87.62.+n, 87.59.-e, 87.59.Bh
Keywords: X-ray phase contrast image, Talbot interferometer, Phase stepping, Diffraction grating
DOI: 10.3938/jkps.65.2111

I. INTRODUCTION

There are two X-ray imaging methods: X-ray absorption and phase contrast techniques. X-ray phase-contrast imaging has attracted great attention over the last decade. Because the interaction cross section of the X-ray phase shift is much larger than the absorption cross section at high X-ray energy, X-ray images of high sensitivity can be made by using phase-contrast X-ray imaging [1, 2]. Applications of this contrast mechanism in X-ray microscopy and bio-medical field are very active [3,4].

Several techniques are now available to exploit and visualize phase contrast imaging: *e.g.*, propagation-based and analyzer-based methods, crystal and grating interferometry, and non-interferometric methods such as a coded aperture [5–7]. Apart from differences in the experimental setups and in the spatial and temporal coherences that are required of the X-ray beam, each method shows differences in the nature and the amplitude of the provided image signal and in the amount of radiation dose delivered to the sample. The grating interferometer is related to the crystal interferometer because both consist of a beam splitter and a beam analyzer, and both have recently been applied to X-ray imaging [8, 9]. Of those methods, X-ray phase imaging using a grating-based interferometer has been actively studied because laboratory X-ray sources can be used, which is a practical advantage.

*E-mail: khy1646@wonkwang.ac.kr; Fax: +82-63-851-4749

A system based on a grating-based interferometer using a conventional X-ray tube requires three gratings: source, phase, and absorption gratings. The source grating is necessary because of the large spot size of a conventional X-ray tube. Demands for an X-ray phase-contrast imaging system using a conventional X-ray tube for biomedical applications has increased [10–12]. However, to date, none is widely used in medical diagnostics, even though some have yielded excellent results for specific problems [13].

In an X-ray phase-contrast imaging system, the fabrication of the grating interferometer is crucial [14,15]. The key components are three gratings with silicon and gold structures that have dimensions in the micrometer range and high aspect ratios. Therefore, the periods and the heights of the gratings and the grating area determine the field of view (FOV) in phase imaging and should be considered. For realizing medical applications, the system for phase-contrast imaging should be a simple as possible, which means reducing the number of gratings. A source grating can be removed by using a micro-focus X-ray tube. For practical uses, a phase-contrast system based on a micro- focus (a few micrometers) tube is not recommended because the tube is very expensive.

In this research, the possibility of using a micro-focus (a few tens of micrometers) tube, which is relatively inexpensive compared to an X-ray tube with a spot size of a few micrometers, in a phase-contrast X-ray imaging system was examined. We developed a grating interferometer system using a laboratory X-ray source to study its imaging performance and to image weakly- absorbing details similar to those often encountered in biology and medicine. In this paper, we describe the design of the Talbot interferometer, the configuration of the experimental setup, and the differential phase-contrast imaging derived from these experiments.

II. MATERIALS AND METHODS

1. Design of Talbot Interferometer

If an X-ray-beam-generated coherent light source (with a wavelength of λ) passes through a diffraction grating (with a period of p), interference fringes having the same period as the diffraction grating appear repeatedly at locations corresponding to integer multiples of $Z_T = 2p^2/\lambda$. In grating-based interferometry, a 0.5π or π phase-shift grating is used mainly as a beam splitter. Especially for π phase-shift gratings, the maximum contrast will occur at $d_1 = 1/16Z_T$, $d_3 = 3/16Z_T$, $d_5 = 5/16Z_T$, $\cdots$ (odd order), which is called the fractional Talbot distance. An imaging detector is placed at this position. A main factor in the design of grating interferometers is the calculation of the Talbot distance, which affects the size of the entire system. Figure 1 shows the configuration of the X-ray Talbot interferometer.

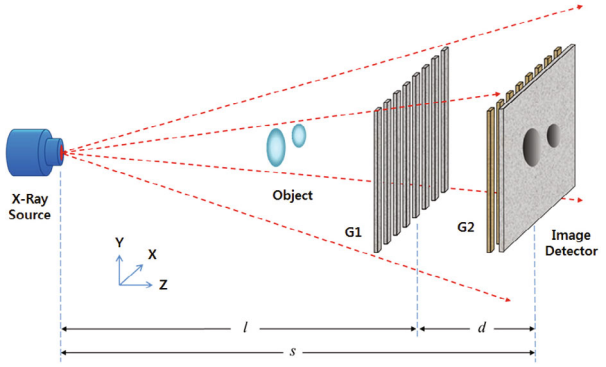

Fig. 1. (Color online) Configuration of a Talbot interferometer based on a micro-focus X-ray tube.

The interferometer consists of a phase grating, G1 (*i.e.*, a grating whose lines show negligible absorption and a substantial phase shift) and an absorption grating, G2. The first grating acts as a beam splitter and divides the incoming beam essentially into the first two diffraction orders. We assume that the distance from the source to G1 is l, that from G1 to G2 is d, and the total system length is s. Then, the fractional Talbot distance D_n for plane wave is

$$D_n = \frac{np_1^2}{8\lambda} \ (n = 1, 3, 5, \cdots), \tag{1}$$

where n is the fractional Talbot order. For spherical waves, the Talbot distance d_n is

$$d_n = MD_n, \tag{2}$$

where M is the magnification factor or the ratio of s to l:

$$M = \frac{s}{l} = \frac{l+d}{l} \ (d = d_n). \tag{3}$$

Substituting Eq. (3) into Eq. (2) and considering d as d_n, we obtain

$$d_n = \left(\frac{l+d_n}{l}\right) D_n, \tag{4}$$

And, therefore,

$$\therefore d_n = \frac{np_1^2}{8\lambda} \frac{l}{l - \frac{np_1^2}{8\lambda}}. \tag{5}$$

The main factors influencing the Talbot distance for plane waves are the wavelength of the source and the period of the phase grating. However, for spherical waves, the distance from the source to the phase grating is also an important factor. The fundamental concept of the method is to detect the positions of the fringes and to use them to determine the shape of the wave front. However, because the pitch of the phase grating (and, thus,

Table 1. Design of the phase-contrast imaging system based on Talbot interferometry.

Specifications	Value
Photon energy (keV)	17.5
P_1: Period of G1 (μm)	4.714
Sidewall material of G1	Si
Sidewall height of G1 (μm)	22.48
$P2$: Period of G2 (μm)	2.399
Sidewall material of G2	Au
Sidewall height of G2 (μm)	20
Substrate material	Si (250-μm thick)
Source to G1 (mm)	2200
G1 to G2 (mm)	39.9
M: Magnification factor	1.02

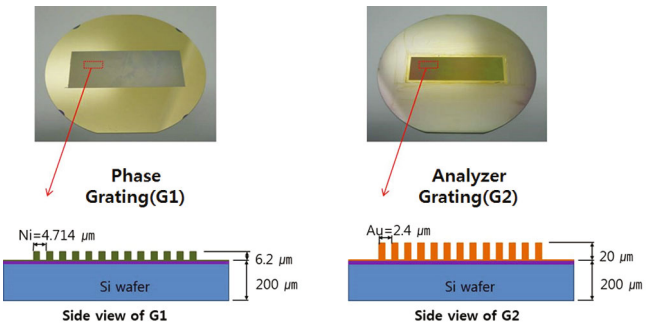

Fig. 2. (Color online) Photographs of a fabricated (a) phase grating G1 and (b) analyzer grating G2, and their conceptual design diagrams.

the spacing of the interference fringes) does not exceed a few microns, an area detector placed in the detection plane will generally not have sufficient resolution to resolve the fringes, let alone the exact positions of their maxima. Therefore, the grating G2 with absorbing lines and the same periodicity and orientation as the fringes is placed on the detection plane immediately in front of the detector. This analyzer grating acts as a transmission mask for the detector and transforms the local fringe position into a signal intensity variation. The detected signal profile, thu, contains quantitative information about the phase gradient of the object. Table 1 shows the design of a Talbot interferometry system employing a grating with a micro-focus X-ray tube. A photon energy of 17.5 keV is considered in the design because it is suitable for medical applications such as breast examination or insect inspection.

Fabricating a grating with dimensions of less than 2 μm is challenging because of the grating's extremely sensitive period. The relational formula between p_1 (the period of G1) and p_2 (the period of G2) is defined as $p_2 = M\frac{p_1}{2}$. The period p_1 that was designed is 4.714 μm, and p_2 is 2.399 μm. Their duty cycles were both 0.5, and

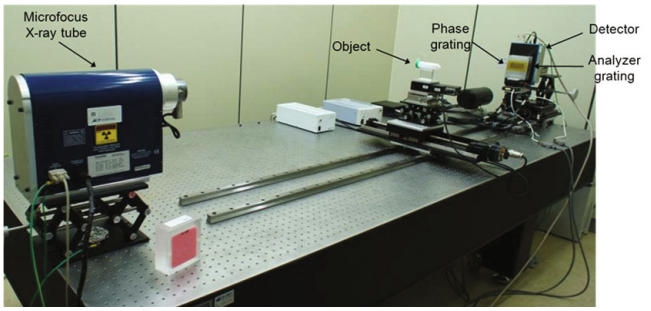

Fig. 3. (Color online) Experimental setup of the X-ray phase-contrast imaging system.

they were fabricated using X-ray lithography of a silicon wafer and, for G2, electroplating with gold by using Microworks GmbH (Karlsruhe, Germany). Figure 2 shows images and diagrams of G1 and G2.

2. Experimental Setup

The system configuration shown in Figure 3 was constructed; it consists of an X-ray generator, an object (specimen), the phase and analyzer gratings, and a detector on an optical table. The experiments were conducted using a micro-focus tube (Kevex PXS10, Thermo Scientific, CA, USA) operated at 38 kV/0.35 mA. The focal spot was 17 μm. We used a CMOS 1512 detector (Dexela, UK) with excellent sensitivity, high-speed image capture, and low noise. The scintillator in the detector system is composed of 150-μm-thick CsI on an amorphous carbon substrate and has a modulation transfer function of 20% at 6 lp/mm. It has a sensitive area of 145.4 × 114.9 mm^2 with a pixel size of 74.8 μm and a dynamic range of 14 bits. The phase grating, G1, was positioned 220 cm from the X-ray source, and the analyzer grating, G2, was positioned 39.9 cm from G1. The distance between G1 and G2 was the first fractional Talbot distance. An object was placed between the X-ray source and G1, 180 cm from the source. An extremely sensitive stage was used to transfer the specimen and to align the gratings. A moiré fringe is formed depending on the state of alignment between G1 and G2, and an precise accurate determination of the alignment of the gratings is possible by measuring this fringe. If the gratings are aligned, the distance between G2 and G1 is adjusted to realize a precise Talbot distance. Then, a very flat field, with no or possibly one moiré fringe, can be observed. When this is realized, experimental work can be performed.

The grating interferometer is designed to create an interference pattern that changes in shape because of the interaction between the X-rays and the sample. The images are recorded by the detector during a phase-stepping scan of the analyzer grating, G2, to reconstruct the interference pattern. The analyzer grating is moved

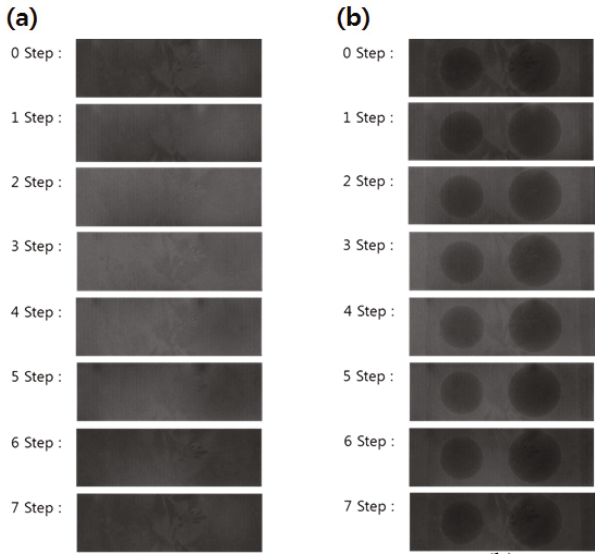

Fig. 4. Images recorded by the detector during a phase-stepping scan for a reference beam (a) without sample and (b) with a sample.

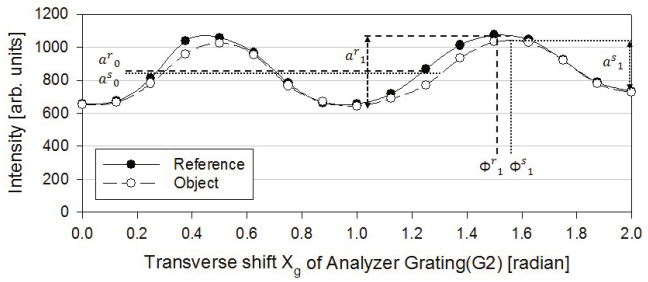

Fig. 5. Intensity curves of the phase shift. The red line with squares indicates the intensity of the reference beam. The green line with triangles indicates the intensity at the left edge of a cylindrical object. Data were fitted with a cosine function. The average value a_0, the shift Φ_1, and the amplitude a_1 of the first-order cosines are indicated.

along the x axis at 0.3 μm/step for a total of eight steps, corresponding to the period of G2. By comparing the interference pattern obtained with the sample in place to that of the reference beam with no sample, we could calculate the refraction angles introduced by the sample. Figure 4 shows eight images recorded for a beam with no sample and the corresponding eight images recorded with a sample in the beam. The intensities of the transverse phase shift of G2 are shown in Fig. 5. For each pixel, an intensity curve can be plotted, where x_g is the transverse shift of the analyzer grating.

3. Image Analysis

The modulation transfer function (MTF) curves of the sample were measured for a quantitative spatial resolution evaluation. The MTF profiles at the boundary of the abdomen of a honey bee were compared with a conventional absorption image and a phase-contrast image (Fig. 6). We obtained normalized values for statistical comparisons of both a conventional absorption image and a differential phase-contrast image. The normalized values from the images were calculated by using the follow-

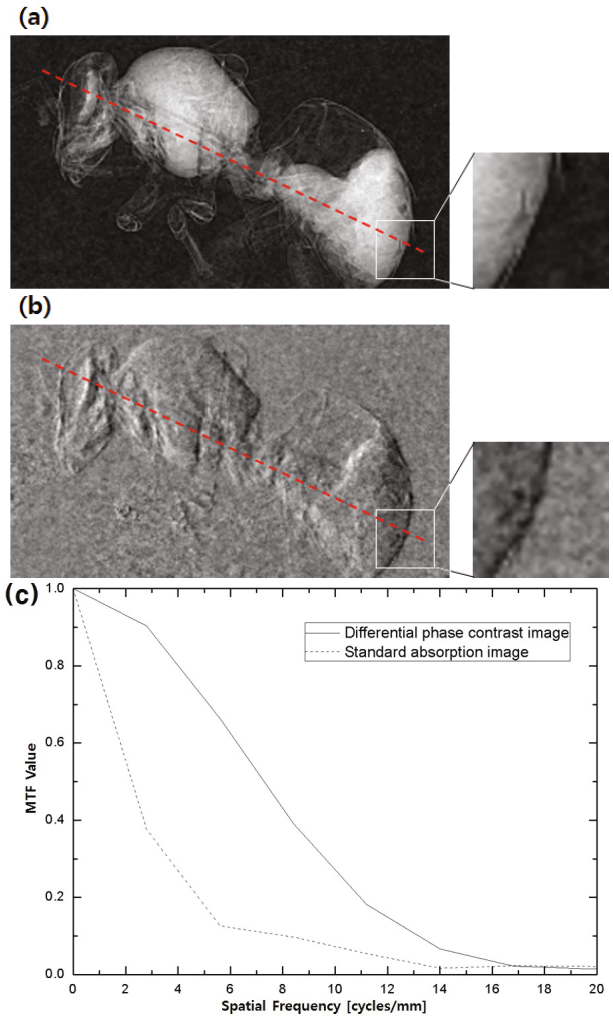

Fig. 6. (Color online) (a) Standard absorption imaging and (b) differential phase contrast imaging of a honey bee. The phase-contrast images were recorded using 8 steps, 45 sec per step, at a photon energy of 17.5 keV and a current of 350 μA. The dashed line and the white rectangle on the images indicate the location for the line profile analysis and the area for MTF analysis (c), respectively. MTF curve along the white rectangle in (a) and (b). MTF profiles acquired at the boundary of a honey bee from a differential phase-contrast image (solid line) and standard absorption image (dashed line). A comparison of the MTF plots of the two images shows that the resolution of the differential phase-contrast image is superior to that of the standard absorption image.

ing equation:

$$\text{Normalized Image} = \frac{(P - I_{min})}{(I_{max} - I_{min})} \quad (6)$$

where P is each pixel value of the image, Imin is the minimum intensity of the image, and Imax is the maximum intensity of the image. Ten positions of the bee, the eye, forefoot, visceral, neck, jaw, head, back, nose, and mandible, were chosen for the analysis. We obtained a profile histogram for each position and image; then, contrast differences of the edge were calculated from the profile histogram. The normalized values were analyzed by using the paired t-test and the statistical package for social sciences (SPSS version 17.0, Chicago, IL, USA) program.

III. RESULTS

As a biomedical application, we obtained absorption and differential phase contrast images of an insect. For these measurements, radiation with a mean photon energy of 17.5 keV and a current of 350 μA was used. Absorption and phase-contrast signals were extracted from a phase stepping scan with 8 frames recorded while stepping the analyzer grating G2. Each frame was recorded with a 25-second exposure time, giving a total exposure time of 200 seconds. The standard absorption contrast and differential phase contrast images of a honey bee are displayed in Fig. 6. In the standard absorption image, only the attenuation of the sample is displayed. On the contrary, in the differential phase-contrast image, the contour of the sample is clearly visible because the refraction from the edges of the object is strong.

The MTF profiles at the boundary of the abdomen of a honey bee are shown in Fig. 6(c). A comparison of the MTF plots of the two images shown that the resolution of the differential phase-contrast image was superior to that of the standard absorption image. The mean normalized value of the edge contrast differences for both the conventional absorption image and the differential phase-contrast image were 0.2807 ± 0.121 and 0.3960 ± 0.131, respectively (Table 2). The edge contrast of the phase-contrast image was superior to that of the absorption image ($p < 0.001$). We obtained absorption and differential phase-contrast images of a grasshopper (Fig. 7). The edge of grasshopper on the phase-contrast images revealed details.

Table 2. Normalized value of the edge contrast differences on the profile of each position of both image techniques.

No.	Position	Absorption Contrast Image	Phase Contrast Image	P-value
1	Eye	0.5338	0.6496	
2	Left forefoot	0.3591	0.5369	
3	Right forefoot	0.2171	0.4611	
4	Visceral	0.2083	0.2531	
5	Neck	0.1238	0.2183	
6	Jaw	0.3152	0.3299	
7	Head	0.2215	0.3617	
8	Back	0.3963	0.4201	
9	Nose	0.2384	0.4157	
10	Mandible	0.1933	0.3135	
	Mean ± SD*	0.2807 ± 0.121	0.3960 ± 0.131	< 0.001

* Abbreviation, SD: standard deviation

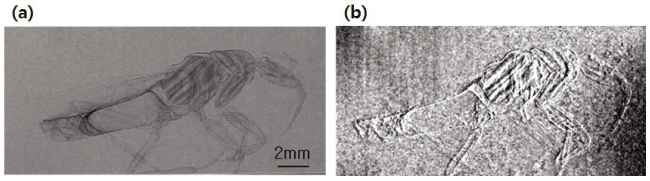

Fig. 7. Images of a grasshopper with (a) standard absorption and (b) differential phase contrast imaging using a microfocus X-ray tube with a photon energy of 17.5 KeV and a current of 350 μA. These phase contrast images were recorded using 8 steps, 25 sec per step. In differential phase-contrast image, the contour of the sample is clearly visible because the refraction from the edges of the object is strong.

IV. DISCUSSION

Phase-contrast imaging has become a paradigm in laboratory X-ray biomedical imaging. With theoretical and technological developments, a grating-based Talbot interferometer could be sufficiently attractive as an X-ray imaging system for generating phase imaging, as we have demonstrated with our experimental results. The strongest advantage of this technology is that the use of laboratory X-ray sources is possible, which is highly significant for biomedical applications [16–19]. Laboratory micro-focus X-ray tubes provide sufficient transverse coherence of the wave front, but the intensity is low.

Our experimental results show that a grating interferometer can be used for X-ray phase-contrast imaging. In principle, the beam grating splits the beam by diffraction, but the diffraction orders are separated by less than a milliradian; hence, the diffracted beams are not spatially separated, but will interfere to create an intensity pattern downstream of the beam splitter at a distance defined by the Talbot effect [7]. The refraction in a sample is measured by detecting the transverse shift of the interference pattern with a high-resolution detector or an analyzer grating. The use of phase stepping provides a method of separating the absorption from the phase signal and easily retrieving the projected phase while preserving the resolution of the imaging system.

Several researchers recently began to explore the pos-

sibility of applying the phase-contrast imaging technique using micro-focus X-ray tubes to breast tissue [20], articular cartilage and bone [21], and materials [22]. However, these studies remain almost completely restricted to the laboratory. In addition, phase-contrast imaging has been used in phase-contrast X-ray tomography [23]. The technique was used with both a grating interferometer and a conventional X-ray tube source and was successfully applied, with a strongly increased contrast-to-noise ratio to the three-dimensional observation of tendons and ligaments. That study demonstrated the potential of phase-contrast computed tomography (CT) for clinical investigations of human specimens and, potentially, humans. A few years ago, we reported the results of a phase-contrast CT experiment aimed at visualizing the knee cartilage in a mouse model of collagen-induced arthritis [24]. The results suggested that phase-contrast imaging using a micro-focus X-ray source for medical applications still had problems that would have to be resolved in the future.

In our study, a grating-based Talbot interferometer seemed to be sufficiently attractive as an X-ray imaging system for generating phase-contrast images. However, the following problems are anticipated if this system is applied to medical use. First, it is difficult to fabricate a large-area analyzer grating with a sufficiently high aspect ratio to secure a large enough FOV and to use high energy. Second, more time is needed to acquire phase-contrast images than to acquire conventional transmission images. Third, the X-ray output from micro-focus X-ray tubes is too weak for use as a clinical source. Although a small focal spot tube could be adequately applied to very small samples, this technology would not be of medical value. If these problems can be overcome, X-ray phase imaging obviously has potential and is expected to soon become a great tool for medical diagnostics.

V. CONCLUSION

In conclusion, we carried out a feasibility study of phase-contrast imaging using a micro-focus X-ray tube (spot size of a few tens of micrometers). A 17-μm micro-focus tube was suitable for use in a grating-based interferometry system without a source grating to obtain phase-contrast images. Our results demonstrate that a grating-based Talbot interferometer may be attractive for use as an X-ray imaging system for generating phase-contrast images.

ACKNOWLEDGMENTS

This work was supported by the Korea Health Industry Development Institute (KHIDI), Grant No. A120152, under the auspices of the Ministry of Health and Welfare.

REFERENCES

[1] T. J. Davis, D. Gao, T. E. Gureyev, A. W. Stevenson and S.W. Wilkins, Nature **373**, 595 (1995).
[2] K. A. Nugent, T. E. Gureyev, D. F. Cookson, D. Paganin and Z. Barneaa, Phys. Rev. Lett. **77**, 2961 (1996).
[3] R. A. Lewis, Phys. Med. Biol. **49**, 3573 (2004).
[4] M. S. Kim, S. W. Oh, J. H. Lim and S. W. Han, Appl. Phys. Lett. **97**, 2137031 (2010).
[5] A. Momose, Jpn. J. Appl. Phys. **44**, 6355 (2005).
[6] A. Yoneyama, T. Takeda, Y. Tsuchiya, J. Wu, T. T. Lwin, K. Hyodo and Y. Hirai, J. Synchrotron Rad. **12**, 534 (2005).
[7] T. Weitkamp, A. Diaz, C. David, F. Pfeiffer, M. Stampanoni, P. Cloetens and E. Ziegler. Opt. Exp. **13**, 6296 (2005).
[8] C. David, B. Nohammer and H. H. Solak, Appl. Phys. Lett. **81**, 3287 (2002).
[9] A. Momose, S. Kawamoto, I. Koyama, Y. Hamaishi, K. Takai and Y. Suzuki, Jpn. J. Appl. Phys. **42**, L866 (2003).
[10] F. Pfeiffer, T. Weitkamp, O. Bunk and C. David. Nature Phys. **2**, 258 (2006).
[11] A. Bravin, P. Coan and P. Suortti. Phys. Med. Biol. **58**, R1 (2013).
[12] J. J. Socha, M. W. Westneat, J. F. Harrison, J. S. Waters and W. K. Lee, BMC Biol. **5**, 1 (2007).
[13] A. Momose, H. Kuwabara and W. Yashiro, Appl. Phys. Exp. **4**, 0666031 (2011).
[14] C. David, J. Bruder, T. Rohbeck, C. Grünzweig, C. Kottler, A. Daiz, O. Bunk and F. Pfeiffer, Microelectron Eng. **84**, 1172 (2007).
[15] D. Noda, M. Tanaka, K. Shimada, W. Yashiro, A. Momose and T. Hattori, Microsyst. Technol. **14**, 1311 (2008).
[16] T. Shibata and T. Nagano, Nat. Med. **2**, 933 (1996).
[17] Y. S. Kashyap, T. Roy, P. S. Sarkar, P. S. Yadav, S. Mayank, S. Amar, K. Dasgupta and D. Sathiyamoorthy, Rev. Sci. Instrum. **78**, 083703 (2007).
[18] E. F. Donnelly, K. G. Lewis, K. M. Wolske, D. R. Pickens and R. R. Price, Phys. Med. Biol. **51**, 21 (2006).
[19] E. L. Ritman, Acad. Radiol. **16**, 909 (2009).
[20] M. Stampanoni *et al.*, Invest. Radiol. **46**, 801 (2011).
[21] D. Stutman, T. J. Beck, J. A. Carrino and C. O. Bingham, Phys. Med. Biol. **56**, 5697 (2011).
[22] S. C. Mayo, A. W. Stevenson and S. W. Wilkins, Materials **5**, 937 (2012).
[23] T. Donath, F. Pfeiffer, O. Bunk, C. Grünzweig, E. Hempel, S. Popescu, P. Vock and C. David, Invest. Radiol. **45**, 445 (2010).
[24] Y. S. Lee *et al.*, Acad. Radiol. **17**, 244 (2010).